Motion-Driven Neural Optimizer for Prophylactic Braces Made by Distributed Microstructures

XINGJIAN HAN*, Boston University, USA / The University of Manchester, United Kingdom

YU JIANG*, Dalian University of Technology, China / The University of Manchester, United Kingdom

WEIMING WANG, The University of Manchester, United Kingdom

GUOXIN FANG, The Chinese University of Hong Kong, China

SIMEON GILL, The University of Manchester, United Kingdom

ZHIQIANG ZHANG, University of Leeds, United Kingdom

SHENGFA WANG, Dalian University of Technology, China

JUN SAITO, Adobe Research, USA

DEEPAK KUMAR, Boston University, USA

ZHONGXUAN LUO, Dalian University of Technology, China

EMILY WHITING, Boston University, USA

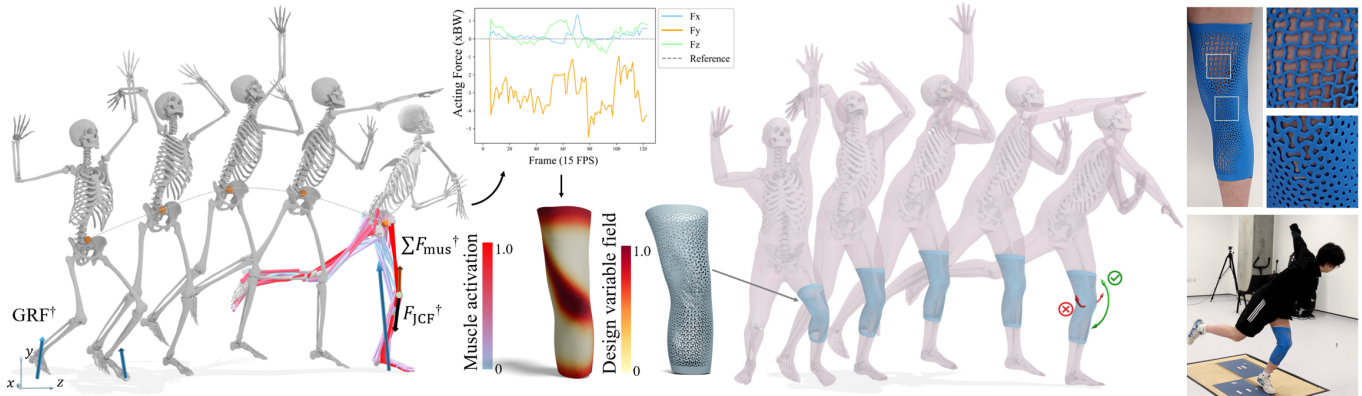CHARLIE C. L. WANG†, The University of Manchester, United Kingdom

Fig. 1. Given an input motion paired with ground reaction forces (GRFs), our approach produces a controlled distribution of elasticity physically realized by microstructures for prophylactic braces. The time-variant load given by kinetic analysis is plotted in the middle, where the frames have been downsampled to 15 fps and the acting forces are normalized to body weight (the testing participant weighs 64 kg). With the help of the optimized brace design, the frontal angles can be effectively reduced while keeping the flexibility of motion throughout the range within sagittal plane.

† The force vectors include the GRF, the joint-contact force and the muscle forces are all scaled down by 0.5× for visualization purposes.

Joint injuries, and their long-term consequences, present a substantial global health burden. Wearable prophylactic braces are an attractive potential solution to reduce the incidence of joint injuries by limiting joint movements that are related to injury risk. Given human motion and ground reaction forces, we present a computational framework that enables the design of personalized braces by optimizing the distribution of microstructures and elasticity. As varied brace designs yield different reaction forces that influence kinematics and kinetics analysis outcomes, the optimization process is formulated as a differentiable end-to-end pipeline in which the design domain of microstructure distribution is parameterized onto a neural network. The optimized distribution of microstructures is obtained via a self-learning process to determine the network coefficients according to a carefully designed set of losses and the integrated biomechanical and physical analyses. Since knees and ankles are the most commonly injured joints, we demonstrate the effectiveness of our pipeline by designing, fabricating, and testing prophylactic braces for the knee and ankle to prevent potentially harmful joint movements.

*Equal contribution of the first two authors.
†Corresponding author

CCS Concepts: • **Computing methodologies → Shape modeling**.

Additional Key Words and Phrases: Motion driven, Computational design, Microstructures, Neural network, Topology optimization

ACM Reference Format:
Xingjian Han, Yu Jiang, Weiming Wang, Guoxin Fang, Simeon Gill, Zhiqiang Zhang, Shengfa Wang, Jun Saito, Deepak Kumar, Zhongxuan Luo, Emily Whiting, and Charlie C. L. Wang. 2024. Motion-Driven Neural Optimizer

for Prophylactic Braces Made by Distributed Microstructures. In *SIGGRAPH Asia 2024 Conference Papers (SA Conference Papers '24), December 3–6, 2024, Tokyo, Japan.* ACM, New York, NY, USA, 12 pages. https://doi.org/10.1145/3680528.3687661

1 INTRODUCTION

In the realm of sports and recreational activities, the potential for injury presents a universal challenge. A well-designed prophylactic brace needs to provide thorough protection without constraining performance. Many current simulation-based design methods (e.g., [Andersen and Rasmussen 2023]) employ a two-stage process by iteratively updating the input of the biomechanical analysis (i.e., the brace designs and the reaction forces) and the input loads of the physical analysis (i.e., the action forces). They require separate phases for initial development and subsequent integration along with manual iterations, which makes it challenging to benefit from the functionality of topology optimization for generating distributed elasticity. [Liu et al. 2023a]. To overcome this limitation, we propose a computational pipeline that enables time-variant topology optimization equipped with kinematics and kinetics analysis (Fig.1). The effectiveness of our approach has been verified by physically fabricated braces through try-on tests and motion evaluations.

While more material may provide more support, distributing coverings over highly mobile regions might restrict mobility [Vechev et al. 2022a]. Our design strategy aims for a balance: crafting a prophylactic brace that offers precise kinematics control of limiting undesired rotation (typically in the frontal plane) while preserving range of motion within the sagittal plane to execute movements safely. To achieve this, we consider both movement patterns (kinematics) and the forces involved (kinetics) in the design with integrated biomechanical and physical analyses. We propose a design optimization for distributing elasticity, fabricated as microstructures in a hyperelastic material. The optimization is parameterized in a neural network with a self-learning process. We implement a carefully designed set of losses combined with integrated biomechanical and physical analyses. The result is a physical brace providing tailor-made prevention and preservation throughout the motion sequence. In summary, our contributions are as follows:

- We investigate a closed-loop differentiable framework that can systematically optimize a customized brace design by integrated biomechanical analysis, physics analysis, and time-variant topology optimization (Sec. 3).
- We develop a formulation that effectively generates distributed microstructures based on the optimized neural function to achieve the desired elasticity distribution (Sec. 4).

We use our pipeline to design prophylactic braces and showcase the applicability of the method through designs with different joint dynamics and conditions.

2 RELATED WORK

2.1 Computational Design of Prophylactic Wearables

Prophylactic bracing is a widely used and practical intervention for preventing the physical consequences of joint injuries. In particular, prophylactic knee braces are designed to control knee motion that is thought to increase the risk of anterior cruciate ligament (ACL)

and other soft tissue injuries at the knee [Tuang et al. 2023]. Reports [Abrams et al. 2012; Majewski et al. 2006] state that lateral collateral ligament and medial meniscus pathology were more frequent in tennis players as compared to other sports. Tuang et al. [2023] suggests reducing peak knee abduction (valgus) angles in the coronal (frontal) plane can potentially lower the risk of noncontact ACL injury. In the sagittal plane, promoting greater knee flexion can reduce the risk of ACL injury as landing with an extended knee with a reduced flexion angle range can increase the load on the ACL. [Myer et al. 2011]. For ankle, prophylactic braces or taping aims to reduce the incidence of injuries like lateral sprains (e.g., [Farwell et al. 2013; Gross and Liu 2003; Hagan et al. 2024; Verhagen and Bay 2010]). These biomechanical insights guide our objective design of precise kinematics control over different planes to ensure joint stability.

Biomechanical simulation tools, such as AnyBody [Andersen and Rasmussen 2023] and OpenSim [Delp et al. 2007], offer a promising avenue for improving the design and optimization with the finite element analysis (FEA) for customization. We employ the biomechanical tools provided by OpenSim [Delp et al. 2007] to realize an end-to-end computational pipeline of motion-driven optimization.

In computational design, research has been conducted for decades to provide compression with customized shape of braces (e.g., [Wang and Tang 2007]). Recently, Zhang and Kwok [2019] used topology optimization to design custom lightweight, high-performance compression casts/braces on two-manifold mesh surfaces, and Zhang et al. [2017] designed personalized orthopedic casts which are thermal-aware. Jiang et al. [2022] demonstrated a customizable ankle brace with tunable stiffness by integrating machine learning. Vechev et al. [2022c] designed passively reinforced kinesthetic garments that resist a single motion and Vechev et al. [2022b] proposed an automatic optimization method to design connecting structures that efficiently counter a range of predefined body movements. However, these existing approaches have yet to consider the influence of reaction forces generated by varied designs of braces on the biomechanical model.

2.2 Topology Optimization

Time-variant topology optimization is crucial for optimizing structures under time-dependent conditions. Unlike the traditional methods developed for static problems, only a few studies can be found in the literature on this topic (e.g., [Jensen 2009; Wang et al. 2020]). Their strategy of space-time extension is employed in our pipeline.

Topology optimization for microstructures was introduced by combining numerical homogenization in Sigmund [1994]. Many algorithms have since been developed to optimize the unit geometry of microstructures for desired performance, e.g. heterogeneous materials [Torquato 2010], functionally graded properties [Radman et al. 2013], and two-scale designs with multi-material microstructures [Zhu et al. 2017]. We employ a strategy similar to Chen et al. [2018] to generate the distributed microstructures with Solid Isotropic Material with Penalization (SIMP) approach.

Recently, the computation of topology optimization has started to employ Neural Network (NN) techniques to leverage benefits such as auto-differentiation and highly parallel computing power. Zhang
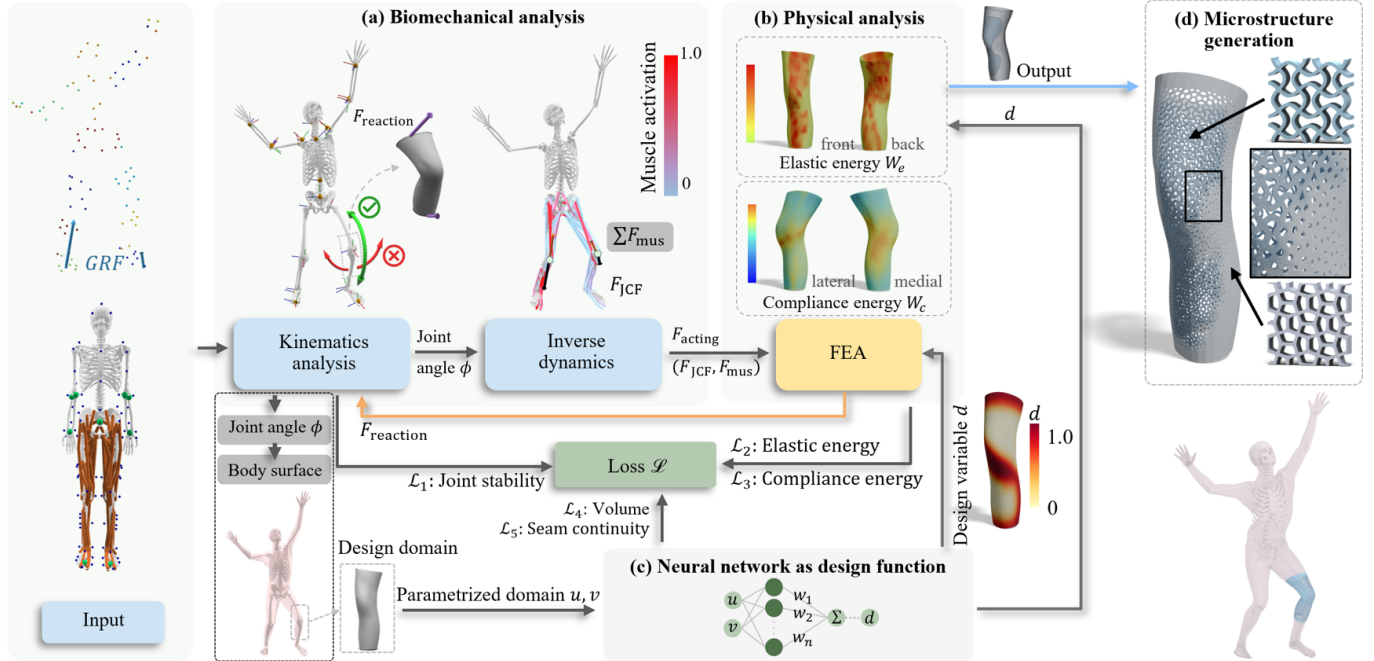
Fig. 2. Overview of our computational pipeline, which includes four major parts: (a) biomechanical analysis (Sec.3.2), (b) physical analysis (Sec.3.3), (c) the *neural network* (NN) based representation of design function (Sec.3.3.1 and Sec.6), and (d) microstructure generation (Sec.4), along with a biomechanical data preprocessing (Sec.3.1, marked in black dotted box). From the input motion sequence and paired ground reaction forces (GRFs), we first conduct a preprocessing step to determine the joint angle, the muscle forces, and the design domain as the body surface with the help of a predefined musculoskeletal model. These terms remain unchanged throughout the optimization (as marked in gray blocks). Our topology optimization process, informed by the time-variant forces F_{acting} given by the biomechanical analysis (a) and governed by the FEA-based physical analysis (b), iteratively updates the NN's weights (c) as design variables to change the distribution of stiffness on a brace while minimizing the compliance energy W_c. In our pipeline, the biomedical analysis and the physical analysis are closely coupled since the reaction force exerted by the braces will further impact the kinematics. The forces generated by a brace at its upper and lower boundaries F_{reaction} are applied to the femur and tibia bones, respectively, prompting updates to the joint contact forces for subsequent analysis. (d) The distributed microstructures for realizing the optimized distribution of stiffness can be generated by first computing the distribution of elastic energy W_e and then filling the regions in low and high elastic energies with the well-blended firm (displayed in light gray) and soft microstructures (displayed in light blue).

et al. [2021] and Chandrasekhar and Suresh [2021] directly optimized the density field alongside the update of NN's weights and bias, this method was recently extended to designing microstructure cells [Sridhara et al. 2022]. Li et al. [2023] introduced a neural representation for generating structures based on directional stiffness and poisson ratio profiles. NN-based computation also offers functional and continuous representation of the design field, facilitating meshless analysis and optimization (e.g., [Zehnder et al. 2021]). Unlike deep neural networks methods, Qian et al. [2023] uses a single layer of Gaussian activation functions, which capture nonlinear features, allowing to optimize fewer neurons (i.e., design variables) and enabling faster convergence. We adopt a similar network architecture.

3 MOTION-DRIVEN NEURAL OPTIMIZER

We introduce a topology design pipeline for prophylactic braces integrated with biomechanical analysis. Our pipeline produces an optimized elasticity distribution given time-variant loads acting on the human body. An overview can be found in Fig. 2. A table of all used symbols can be found in the appendix (Table. 4).

3.1 Data Processing

3.1.1 Inputs. The paired motion capture (MoCap) data of 96 markers to describe full-body motion and corresponding ground reaction forces (GRF) are used as the input for defining movement and the external force resulting from the body's contact with the ground [Han et al. 2023]. We customize a musculoskeletal model (Fig. 3(a)) from [Bedo et al. 2020; Lerner et al. 2015] with $N = 41$ degrees of freedom (DoF) including 3 DoFs for each knee. The model contains 80 Hill-type muscles to evaluate the muscle forces. We customize the locations of markers to ensure alignment with body positions, thereby enhancing the accuracy of the kinematic analysis.

3.1.2 Kinematics and optimization objectives. From the MoCap and GRF data, we employ OpenSim [Delp et al. 2007] and AddBiomechanics [Werling et al. 2023] to calculate the joint angles from marker trajectories by inverse kinematics (IK), with $\phi \in \mathfrak{R}^N$ representing the joint angles. Through optimization, we track joint angle changes in response to the additional reaction force exerted by the braces. We aim to restrict the movement in the frontal plane by minimizing the knee abduction/adduction and ankle inversion/eversion, as they can lead to joint instability and injuries like ACL tears or ankle
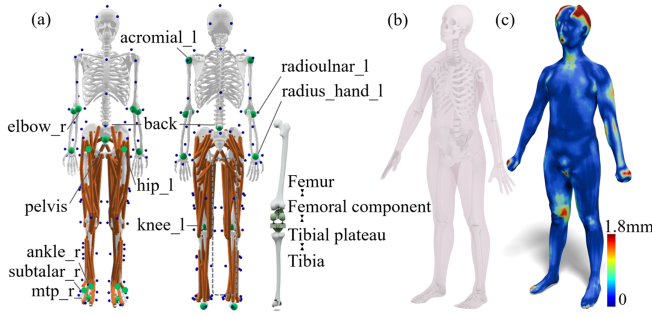
Fig. 3. (a) Overview of the biomechanical model and the marker layout alignment for kinematics and kinetics analysis, where we customize a detailed knee compartment model [Bedo et al. 2020; Lerner et al. 2015] by equipping both knees with three DoFs and adjusting the marker layout (with 96 markers as shown with blue dots) to accommodate more detailed kinematics. (b) From the musculoskeletal model, we extract the outer skin surface by fitting it to the SKEL model $(\beta, \mathbf{q})$ [Keller et al. 2023], where the shape parameters β are obtained from the scanned body as shown in (c) to estimate detailed deformations. The color map measures the shape approximation error between the scanned and updated SKEL bodies.
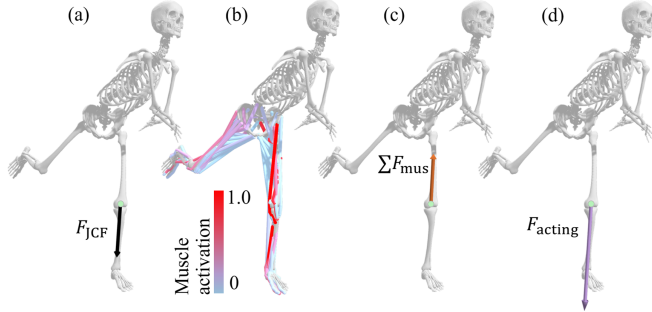

Fig. 4. We show the kinetic analysis of an example left knee joint during the tennis serve motion, specifically at the landing pose. The biomechanical dynamic analysis can estimate (a) the joint contact forces, F_{JCF}, acting on the tibia bone, (b) the muscle activations and (c) the sum of muscle forces $\sum \mathbf{F}_{mus}$. The acting force (d) can then be computed as Eq. (1), which serves as the load input for the integrated FEA. Our optimizer considers the entire sequence of a complex motion, such as tennis serving, which includes several critical phases such as deep bending knees, jumping, and landing.

sprain. Conversely, maintaining a full range of motion in the sagittal plane is essential to safeguard the human body, particularly during landing; these sagittal angles are the ones we aim to preserve. Note that different protocols and third-party software, Visual3D [HAS Motion, Inc. 2024], are employed for results verification in Sec 7.3.

3.1.3 *Body reconstruction.* Extracting the outer skin surface directly from a musculoskeletal model is challenging due to complex anatomy and dynamic deformation introduced by motions. To address this, we employ the SKEL model $(\beta, \mathbf{q})$ [Keller et al. 2023], which defines a parametric body model with corresponding skin and skeleton meshes. $\beta = [\beta_1, ... \beta_{10}]$ is the shape parameters, and

$\mathbf{q} \in \mathbf{R}^{46}$ is the pose parameters representing 46 DoFs of the articulated body. We select some specific regions from the extracted body surface to construct the design domain (Fig. 2). This allows us to analyze the impacts of motion / forces acting on the targeted areas.

3.1.4 *Parametrization for brace design.* Customized braces can be simplified as two-manifold designs on a surface with uniform thickness. These designs are parameterized onto a domain as $(u, v) \in [0, 1]$ using the least squares conformal maps [Lévy et al. 2023]. This reduces the dimensionality of the design domain, making it easier to conduct physical analysis and the generation of distributed microstructures. For taking FEA, the domain is tessellated into a triangular mesh $\mathcal{M}$. Note that the initial relaxed state of the body mesh instead of a deformed mesh is employed for parameterization in our implementation. Moreover, introducing a cutting line is necessary when parameterizing a brace surface resembling a cylinder onto a 2D plane. Constraints are added during the optimization to ensure the design variables at both sides of the cut are consistent.

3.2 Biomechanical Analysis

During human motion, forces and torques (or moments) acting across a joint are derived from external (ground reaction forces) and internal (body weight, muscle forces, soft tissue forces, joint contact forces) sources. At any given instant in time, the dynamic equilibrium is defined as $\sum \mathbf{F} = m\mathbf{a}$ and $\sum \mathbf{M} = I\alpha$ with body segments' mass m, acceleration $\mathbf{a}$, inertia I, and angular acceleration α. Braces can generate reaction forces as additional external sources that alter the magnitude of other components of the dynamic equilibrium.

3.2.1 *Joint contact forces.* A joint contact force ($\mathbf{F}_{JCF}$), as shown in Fig. 4(a), represents the actual load transmitting between bones within a joint. While directly measuring the contact force is difficult, we model the contact with Delp et al. [2007] similar to Lerner et al. [2015] and Bedo et al. [2020] as shown in Fig. 3(a) to extract compressive force acting on the tibia bones for the knee and on the talus bones for the ankle joints. We compute $\mathbf{F}_{JCF}$ with *joint reaction analysis* (JRA) [Delp et al. 2007] given the kinematics and the external loads defined by GRF and the brace reaction forces.

3.2.2 *Muscle forces.* Muscles play a crucial role in supporting and stabilizing joints. A prophylactic brace can supplement muscle by sharing the load. Following Delp et al. [2007] and Feng et al. [2023], we model the muscle as polylines. Muscle activation falling in the range of $[0, 1]$ determines the level of contraction in a muscle, which is used to estimate the muscle forces. During the computation, we only consider the muscles traversing through the joint. The direction of the net muscle force is determined by considering each involved muscle line. We denote the sum of the muscle forces as $\sum \mathbf{F}_{mus}$.

3.2.3 *Overall acting force.* The overall input forces for FEA are the net loads acting on the joint, accounting for both passive (due to the joint and body weight) and active (due to muscle support) components. Specifically, we define the force as follows, and the acting force serves as time-variant loads for FEA:

$$\mathbf{F}_{acting} = \mathbf{F}_{JCF}(\mathbf{F}_{GRF}, \mathbf{F}_{reaction}) - \sum \mathbf{F}_{mus} \tag{1}$$

With these boundary conditions, we can formulate the optimization problem to compute the optimized topology for distributed elasticity.

3.3 Motion-driven Topology Design

Traditional topology optimization algorithms focus on spatial design domains, such as density fields. However, they may not be directly applicable or efficient for addressing time-variant loading problems arising from kinesthetic brace designs. This limitation stems from the high computational cost associated with variable-time nonlinear physical models and the non-convex nature of the design space [Cai et al. 2023]. Developing or adapting algorithms to efficiently navigate this complex landscape remains challenging. Therefore, we integrate the space field with the motion frame, concurrently addressing them through discretization and optimization within a framework.

3.3.1 Time-variant Topology Optimization Model. By borrowing the concept of the density-based SIMP method [Sigmund 2001], we construct the time-variant topology optimization driven by action forces obtained from the kinematics and kinetics analysis. The design domain $d(u, v)$ (similar to 'density' concept in SIMP) is represented by a neural network (NN), which is parameterized by the network coefficients θ. For numerical computation, the SIMP-like optimization is conducted by tessellating the whole domain into finite elements. The design variable d_e in each element e is chosen by the field value at the center of e, where different values of d_e will be mapped to different volume fractions and mechanical properties. In motion-involved scenarios, loads and body surface can change with time; the time-variant loads can be represented as $\mathbf{F}(t)$ with a total of N_t frames sampled at the rate of 15 fps as shown in Fig.1. The walking motion shown in Fig. 9 is sampled at 60 fps.

The time-variant topology optimization problem can then be solved by minimizing the 'worst' compliance energy as:

$$\min_d \max_{\{t_i\}} \quad \left\{ \frac{1}{2} \mathbf{U}^T \mathbf{K}(d) \mathbf{U} \right\} \tag{2}$$

$$\text{s.t.} \qquad \mathbf{K}(d)\mathbf{U} = \mathbf{F}_{\text{acting}}(t_i), \sum_{e=1}^{N_l} \left(f_V(d_e) \cdot V_e \right) \leq V_0,$$

with $e = 1, 2, ..., N_l, i = 1, 2, ..., N_t$, where N_l is the number of elements, $f_E(.)$ and $f_V(.)$ are the functions of the Young's modulus and the volume ratio related to the design function $d(\cdot)$, $\mathbf{K}$ and $\mathbf{U}$ are the global stiffness matrix and nodal displacement vector for FEA. The FEA is conducted by planer elements equipped with the rotation matrix between 3D surface and its corresponding region in the u, v-domain. Specifically, we use MITC3 shell elements (Mixed Interpolation of Tensorial Components) as described in [Lee and Bathe 2004] for our FEA implementation, which is a linear shell model. The stiffness matrix is defined as $\mathbf{K}(d) = \cup_e (f_E(d_e) \cdot \mathbf{k}_0)$ following [Chi et al. 2021] with $\cup_e$ denoting the element assembly. This includes MITC3 shell element's stiffness matrix $\mathbf{k}_0$, and output of Young's modulus function $f_E(d_e)$, with the detailed function given in Sec.4.3 . The MITC3 element accounts for the thickness dimension and includes an additional internal node to capture the bending behavior. Note that the boundary condition of fixing the nodes on the boundaries of a brace needs to be imposed for FEA. V_0 is the allowed maximal volume, V_e is the volume of element e, and

$\mathbf{F}_{\text{acting}}$ indicates the applied nodal force, and d_e is the design variable of the element e. The discrete compliance on each element e can be defined as $W_c = f_E(d_e) \cdot \mathbf{u}_e^T \cdot \mathbf{k}_0(t_i) \cdot \mathbf{u}_e$ with $\mathbf{u}_e$ being the nodal displacement of element e. We further employ p-norm method to approximate the maximum compliance across all the N_t frames as given in Table 1, Sec. 5. The reaction force can be computed by the displacement $\mathbf{U}(t_i)$ and the acting force $\mathbf{F}_{\text{acting}}(t_i)$ as

$$\mathbf{F}_{\text{reaction}}(t_i) = \mathbf{K}(d)\mathbf{U}(t_i) - \mathbf{F}_{\text{acting}}(t_i) \tag{3}$$

This reaction force serves as the brace support and acts back to the body to update the joint angles ϕ and the joint contact forces $\mathbf{F}_{\text{JCF}}$ sequentially with embedded solvers of OpenSim [Delp et al. 2007], where the brace reaction forces are initiated with small values and updated during optimization with automatic differentiation supported by [Andersson et al. 2018; Falisse et al. 2019].

3.3.2 Elastic Energy Based Segmentation. We employ elastic energy density to estimate the degree of local deformation on the time-variant surfaces of human body. To alleviate the constrained movement caused by the brace wrapping, we aim to minimize the total elastic energy on the brace. The distribution of elastic energy can be commonly evaluated by the design function $d(\cdot)$ and the deformation of elements on a brace among different frames. Specifically, given $\mathbf{G}_e(t_i)$, the deformation gradient [Sumner and Popović 2004] of the element e at the time frame t_i w.r.t. its rest shape, the elastic energy W_e at every element can be evaluated with the classical compressible neo-Hookean model [Bonet and Wood 2008] as

$$W_e = \max_{\{t_i\}} \left\{ \frac{\mu_e}{2} (I_e(t_i) - 2) - \mu_e \log A_e(t_i) + \frac{\lambda_e}{2} (\log A_e(t_i))^2 \right\} \tag{4}$$

where $I_e = tr(\mathbf{C}_e)$ is the first invariant of the right Cauchy-Green tensor $\mathbf{C}_e = \mathbf{G}_e^T \mathbf{G}_e$, and $A_e = \det(\mathbf{G}_e)$ is the relative area change. $\lambda_e = v \frac{f_E(d_e)}{(1+v)(1-2v)}$ and $\mu_e = \frac{f_E(d_e)}{2(1+v)}$ are the Lamé's first parameter and the shear modulus respectively, and v is the Poisson's ratio. Both are influenced by the design function $d(\cdot)$. Note that the maximal elastic energy among all relevant frames is employed here.

By the distribution of elastic energy W_e (see the right figure), we segment the entire design domain into the soft and firm regions by the self-tuning spectral clustering method [Zelnik-Manor and Perona 2004] so that different types of microstructures can be assigned into these regions respectively (ref. [Liu et al. 2023b]).

When fabricating the braces with the same super-elastic material (i.e., silicone in our trials), we leverage the strength and stiffness of the microstructures type with high-stiffness in the region with low elastic energy and meanwhile also benefit from the flexible deformation characteristics of the type with low-stiffness in the region with high elastic energy. We introduce details of generating distributed microstructures with different stiffness in Sec.4
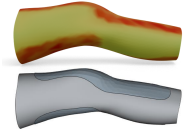
4 DISTRIBUTED MICROSTRUCTURES

4.1 Periodical formulation

Different types of microstructures can be represented with the help of an implicit function $f_{cell}(\hat{u}, \hat{v})$ defined as the distance field to the skeletons in a unit parametric domain $(\hat{u}, \hat{v}) \in [0, 1] \times [0, 1]$. The
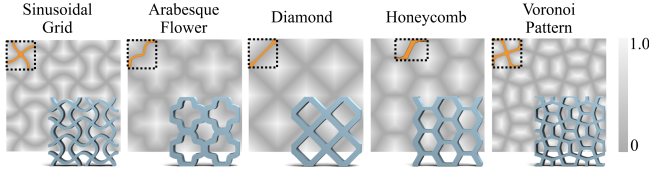
Fig. 5. Different types of microstructures are studied in our research. We provide structures represented by an implicit surface $f_{cell}(\hat{u}, \hat{v})$ in the u, v-domain, and the corresponding solids obtained by $f_{cell}(\hat{u}, \hat{v}) \leq 0.2$ with a user-specified thickness are displayed in blue at the bottom right corner. The function $f_{cell}(\hat{u}, \hat{v})$ is formulated as the distance field to the skeletons (highlighted by curves in orange).

implicit solid of the distributed microstructures in the domain with design variable $d(u, v)$ can be formulated by a periodic function as

$$f_M(d(u,v), u, v) = d(u,v) - f_{cell}(\hat{u}, \hat{v}) \qquad (5)$$

with $\hat{u} = \arccos(\cos 2u\pi/s)/\pi$, $\hat{v} = \arccos(\cos 2v\pi/s)/\pi$, and s being the scale coefficient of an unit cell in the u, v-domain. The implicit solid of distributed microstructure can then be obtained as $\{(u, v) \mid f_M(u, v) \leq 0\}$ – see Fig.5 for five different types of microstructures when $d(u, v) = 0.2$. Some similar structures can be found in Schumacher et al. [2018]. The value of scale coefficient $s = 0.08$ is determined by experiments and employed in all examples in this paper. Note that the function of volume ratio $f_V(\cdot)$ for different types of microstructures is obtained by sampling different values of d and evaluating the volumes of resultant implicit solids. The function $f_V(\cdot)$ is then approximated by a cubic polynomial.

4.2 Mechanical property

Young's modulus plays a vital role, it indicates a material's stiffness and elasticity [Murugan 2020]. Different types of microstructures possess Young's modulus with a broader range than those of conventional materials, which is ideal for designing prophylactic braces.

Young's modulus for microstructures can be approximated by homogenized elasticity tensors. We have evaluated Young's modulus of five types of microstructures shown in Fig.5 by the method presented in Körner and Liebold-Ribeiro [2014]. Curves between Young's modulus and volume ratio, generated using 25 sample points and Least-Squares fitting with an approximation error less than 1e-4, are shown on the right. It can be observed that the *Voronoi Pattern* structure contains the highest Young's modulus with the same volume ratio, whereas the *Sinusoidal Grid* structure gives the lowest

Young's modulus. Following the strategy adopted in Watts et al. [2019], we use a cubic polynomial function to fit Young's modulus function $f_E(\cdot)$ depending on the design variable d. The resultant continuous and homogeneous Young's modulus functions

for both the soft and the firm microstructures are then applied to conduct FEA in Eq.(2) for design optimization, where the volume constraint is controlled with the help of the function $f_V(\cdot)$.
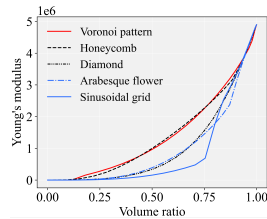
Table 1. Losses for Our Optimization Pipeline

Loss	Formulation
Joint Stability	$\mathcal{L}_1 = \sum_{s \in S_{preserve}} (\tilde{\phi}_s - \phi_s)^2 + \sum_{s \in S_{prevent}} \tilde{\phi}_s^2$
Elastic energy density	$\mathcal{L}_2 = \sum_{e=1}^{N_I} W_e$
Compliance	$\mathcal{L}_3 = \frac{1}{2} (\sum_{j=1}^{N_t} (\sum_{e=1}^{N_I} W_c(d_e, t_i))^p)^{\frac{1}{p}}$
Volume fraction	$\mathcal{L}_4 = (\sum_{e}^{N_I} (f_V(d_e) \cdot V_e)/V_0 - 1)^2$
Seam Continuity	$\mathcal{L}_5 = \sum_{(i,j) \in \mathcal{D}} (d_i - d_j)^2$
Total Loss	$\mathcal{L}_{total} = \omega_1 \mathcal{L}_1 + \omega_2 \mathcal{L}_2 + \omega_3 \mathcal{L}_3 + \omega_4 \mathcal{L}_4 + \omega_5 \mathcal{L}_5$

Table 2. List of symbols employed in the loss functions

| Term	Explanation
$S_{preserve}$	Set of DoFs that need to be preserved (e.g. sagittal angles)
$S_{prevent}$	Set of DoFs that need to be controlled (e.g. frontal angles)
$\tilde{\phi}_s$	Updated joint angle for s given the reaction as defined in Eq.(3)
ϕ_s	The target joint angle for s
W_e	The elastic energy on an element e as defined in Eq.(4)
p	The parameter for p-norm method ($p = 20$ in our trials)
$\mathcal{D}$	The pairs of corresponding points on the cutting line
d_i	The value of design variable on the i-th node of the mesh $\mathcal{M}$
d_e	The design variable sampled at the center of an element e

4.3 Blending dual microstructures

After segmenting the design domain of a brace into soft and firm regions with the help of elastic energy obtained by Eq.(4), we generate a blending map $f_{seg}(u, v)$ by assigning $f_{seg}(u, v) = 0$ for the soft region and $f_{seg}(u, v) = 1$ for the firm region, and a scale (0,1) for the blended regions. To ensure a smooth transition, the boundary values of $f_{seg}(u, v)$ between soft and firm regions are smoothed. The implicit solid can be defined by blending as

$$f_{\bar{M}}(d(u,v), u, v) = \begin{bmatrix} 1 - f_{seg}(u,v) \\ f_{seg}(u,v) \end{bmatrix}^T \begin{bmatrix} f_{M,soft}(d(u,v), u, v) \\ f_{M,firm}(d(u,v), u, v) \end{bmatrix} \qquad (6)$$

where $f_{M,soft}(u, v)$ and $f_{M,firm}(u, v)$ are the functions of the soft and firm microstructures respectively. We blend the Young's modulus the similar way, with the function $f_{\bar{E}} = (1 - f_{seg})f_{E,soft} + f_{seg}f_{E,firm}$, and $f_{E,soft}$ and $f_{E,firm}$ are the functions of the soft and firm Young's modulus respectively. Such blending of Young's modulus will introduce some error but in a very small surface region.

The right figure shows the comparison with (bottom) vs. without (top) the blending formulation. Note that the width of the blended region needs to be controlled due to the inaccuracy of Young's modulus of the blended microstructures. The microstructures as a distribution optimized on a brace can be seen in Fig. 2(d). The resultant solid can be obtained by first extracting a mesh with $f_{\bar{M}}(d(u,v), u, v) \leq d$ on the human body surface and then thickening the surface mesh

into a solid [Wang and Chen 2013; Wang and Manocha 2013].
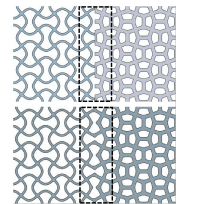
5   LOSS FUNCTIONS

Our optimization model aims to minimize the total elastic energy and compliance with reference to the acting force while considering the joint stability under the prescribed volume fraction. We define each loss term in Table 1 where the definition of relevant symbols are listed in Table. 2. The total loss is defined by combining all terms that are normalized by their initial loss values.

Note that increasing the rigidity of the brace to prevent frontal angle may decrease the sagittal angle (restrict knee flexion), which leads to a trade-off of joint stability and mobility. Our design of loss function allows us to consider supportiveness and motion flexibility on a brace design concurrently. For practical implementation, seam continuity is considered by maintaining consistent design variables at both sides of a cutting line. Additionally, we incorporate total volume fracture loss for the lightweight nature of braces. Note that we only observed a very trivial discontinuity of $d(\cdot)$ across the cutting line in all examples if not applying this loss. However, the value of compliance loss $\mathcal{L}_3$ will be increased if the discontinuity is not penalized. Therefore, a very small weight $\omega_5 = 0.02$ is employed for the seam continuity loss while the other weights are chosen by experiments as $\omega_1 = 0.5$, $\omega_2 = 0.8$, $\omega_3 = 0.6$ and $\omega_4 = 0.3$.

6   NETWORK ARCHITECTURE

The aim behind introducing neural networks to present the distributed microstructures is to create a differentiable design function $d(\cdot)$ for a gradient-based optimizer. Specifically, $d(\cdot)$ is defined as a single layer neural-network:

$$d(w_1, w_2, ..., w_{N_w}) = \sum_i^{N_w} w_i \psi_i(u, v), \qquad \sum_i^{N_w} w_i = 1 \qquad (7)$$

with N_w being the number of neurons. The neural weights $\{w_i\}$ are the variables of the optimizer to influence terms defined in the loss function while serving as the differentiable representation for microstructures. In our implementation, the Gaussian covariance $\psi_i(u, v) = \exp\left(-\sigma^2((u - u_i)^2 + (v - v_i)^2)\right)$ with $\sigma = 4.0$ is chosen as the activation function because of its high flexibility and adaptability to non-linear data distributions. The centers of activation functions are obtained by uniformly sampling the u, v-domain into N_w points. In addition, the projection is placed behind the single layer NN in order to keep the design function d within the range $[0, 1]$. For the sake of easy to converge, a single layer NN is employed in our implementation with $N_w = 10,000$ neurons. The framework can be further extended to capture higher nonlinear variation in the design space by using multiple layers of neurons.

7   RESULTS AND VALIDATION

We demonstrate our pipeline by analyzing and designing solutions tailored for different joint conditions and varied movement patterns. We fabricate the braces with Silicon rubber with 30A stiffness and verify their performance via physical try-on.

7.1   Design for Prophylactic Braces and Ablation Study

We first design a pair of knee prophylactic braces for tennis serving motion (see Fig. 1 and Fig. 9(a)). During tennis serving that includes the phases of deep knee bending, jumping, and landing, a tennis
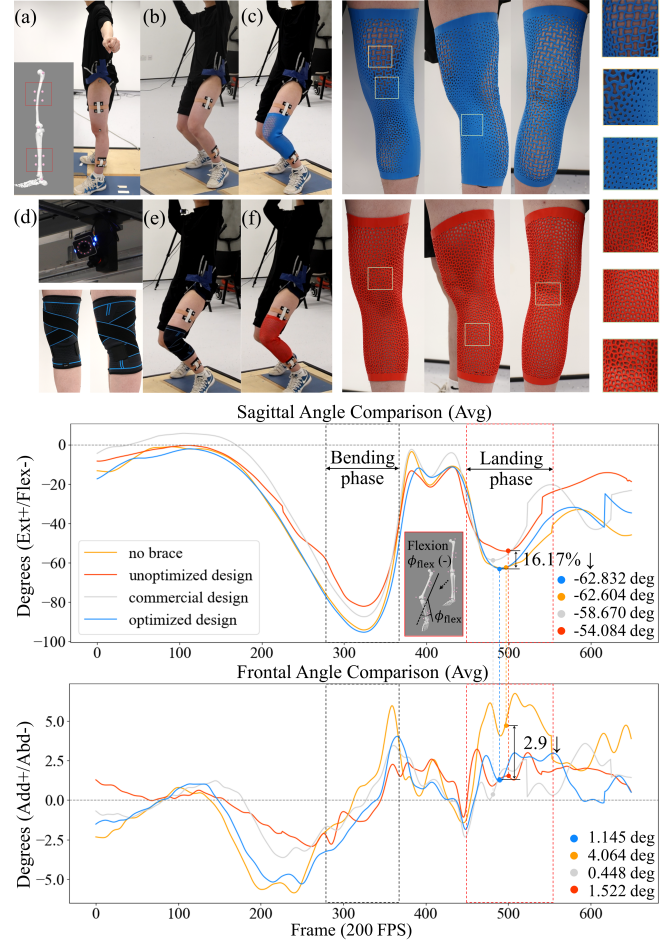

Fig. 6.   Physical validation of prophylactic brace for the left knee. Left: (d) Motion capture system with twelve Vicon Vero 13 cameras. (a) Motion capture protocol for 13 markers placed on left lower extremity: 2 clusters on femur and tibia – each with 4 markers (see red boxes), which are used to compute knee angles. Five more calibration markers located on left hip, lateral and medial of left knee and ankle to identify joint and body segments. The participant repeats the tennis serving motion 5 times for (b) unbraced, (c) wearing our optimized brace, (e) a commercial prophylactic brace and (f) an unoptimized brace with uniform 'Voronoi Pattern' microstructure. Right: plot of joint angles for comparison, which are obtained from the average of synchronized curves for each case. Note the peak flexion is used for alignment and the second peak flexion is selected for comparing the angles for both planes at the landing moment, as this passive action can elevate the risk of joint injury, especially if the knee lacks adequate flexibility and remains extended upon landing. Our optimized design yields similar support as the uniform stiff patterns (reduced) and commercial braces while providing more flexibility within the sagittal plane, which is important to allow more bending upon contact with the ground.

layer can exert forces (normalized by the body weight) on their joints as shown in the force plots of Fig. 1. In the second example, we analyze the kinetics and design bilateral knee braces for gait (see Fig. 9(b)). Our optimizer effectively considers the asymmetry of the
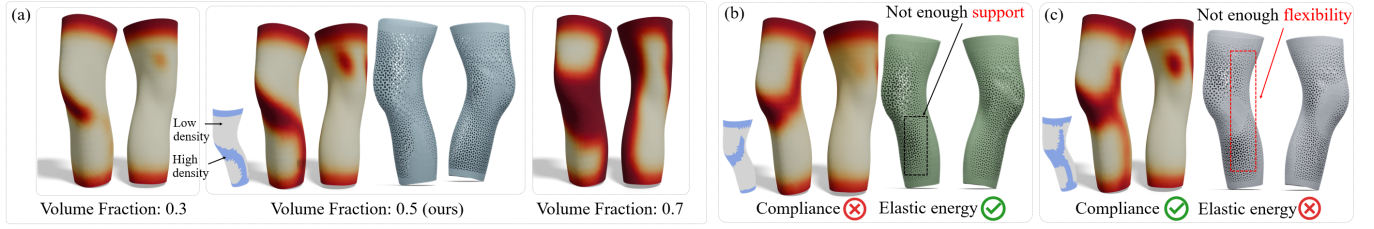
Fig. 7. Ablation study for the necessity of different loss terms: (a) The loss term of volume fraction $\mathcal{L}_4$ is employed to control the amount of materials used for the braces – the volume fraction 0.5 is employed for all other examples in this paper, (b) removing the compliance loss $\mathcal{L}_3$ will generate a brace with less support to prevent the adduction – the upper & lower loops of the brace are not connected by high-density regions, and (c) the flexibility of movement is not preserved without the loss of elastic energy density $\mathcal{L}_2$ which leads to a result with extra connection from the knee to the upper loop by a high-density region.
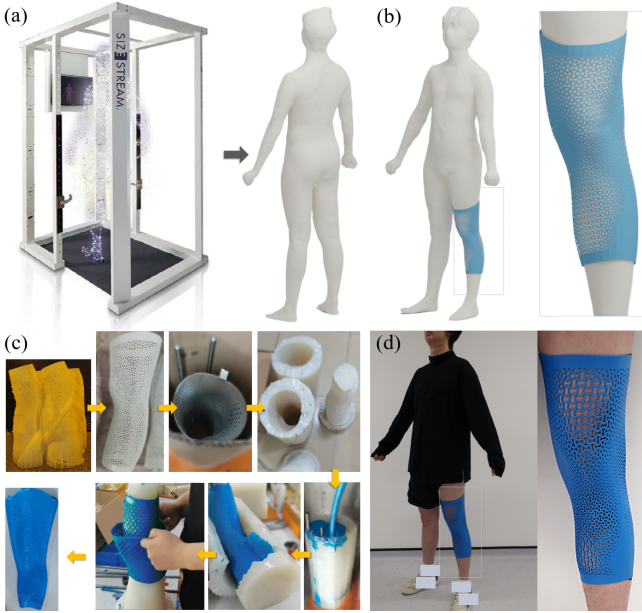

Fig. 8. To ensure the brace can be properly worn, we first capture the participant's body by a structure-light based scanner (online image resource accessed May 2024) and reconstruct the 3D surface (a). The optimized design of a knee brace is computed in a user-specified region (b). The designed brace with microstructures are generated by offsetting [Wang and Manocha 2013] and fabricated by Silicon rubber with 30A stiffness using a casting method with the 3D printed mold (c). (d) A physical try-on is provided with a zoom-in view on the right.

body and provides targeted support at the lateral of the knee for both sides. In the other example (see Fig. 9(c)), as different loads are applied to different joints, we also analyze the dynamics of the ankle for a tennis serving motion to generate customized ankle braces.

Furthermore, ablation studies have been conducted to illustrate the necessity of loss terms (see Fig. 7). The compliance loss $\mathcal{L}_3$ is important to provide enough support by controlling the frontal angle, and the elastic energy loss $\mathcal{L}_2$ can help effectively keep the flexibility in the sagittal plane. Removing the compliance loss $\mathcal{L}_3$ will generate a brace without direct connection (by high-density regions) between the upper and lower loop of the brace – i.e., not enough

Table 3. Joint angle comparison for physical verification at bending and landing moments

Brace condition	Bending Sagittal[†]	Bending Frontal[‡]	Landing Sagittal[†]	Landing Frontal[‡]
Unbraced [*]	0	0.825	0	16.519
Unoptimized brace (Fig.7(b))	1.413	1.990	28.141	11.39
Unoptimized brace (Fig.7(c))	78.049	4.045	33.091	7.537
Unoptimized brace (Fig.6(f))	144.148	1.782	72.579	2.315
Commercial brace	44.788	**0.076**	15.478	**0.200**
Optimized brace (ours)	**1.374**	0.526	**0.052**	1.310

[†] Sagittal angle with extension (+) and flexion (-) is compared with [*]. A sagittal angle close to unbraced condition suggests angle preservation.
[‡] Frontal angle with adduction (+) and abduction (-) is compared with *zero*. A frontal angle close to zero is indicative of more joint stability within frontal plane.

support. On the other aspect, without the elastic energy loss $\mathcal{L}_2$, the design adds extra high-density regions, creating extra restriction to the movement. All these differences in the pattern topology of high-density regions are visualized in Fig. 7 and quantative results are provided in Table.3.

7.2 Physical Try-on

We fabricated the prophylactic braces for the left knee joint tailored to tennis-serving motion with silicone. Given the body surface of the scanned participant (Fig. 8(a)), we obtain the shape parameters, β of the SKEL [Keller et al. 2023] model by optimizing the parameters with a template human body to minimize the distance between two mesh surfaces. We conduct optimization on $(\beta, \mathbf{q})$, where the pose parameters $\mathbf{q}$ is from Han et al. [2023]. Our optimized design conforms to the scanned body during physical try-on. The comparison of the scanned surface and fitted SKEL is shown in Fig. 3(c) and the detailed fabrication and try-on process can be found in Fig. 8(c, d).

7.3 Verification

While the software solution for simulating the musculoskeletal model with the optimized brace model with distributed microstructures is challenging, we directly conduct physical experiments to validate the performance of optimized braces generated by our approach (see Fig.6). We test the fabricated left knee brace for a tennis player and evaluate the joint angles from the mocap data during
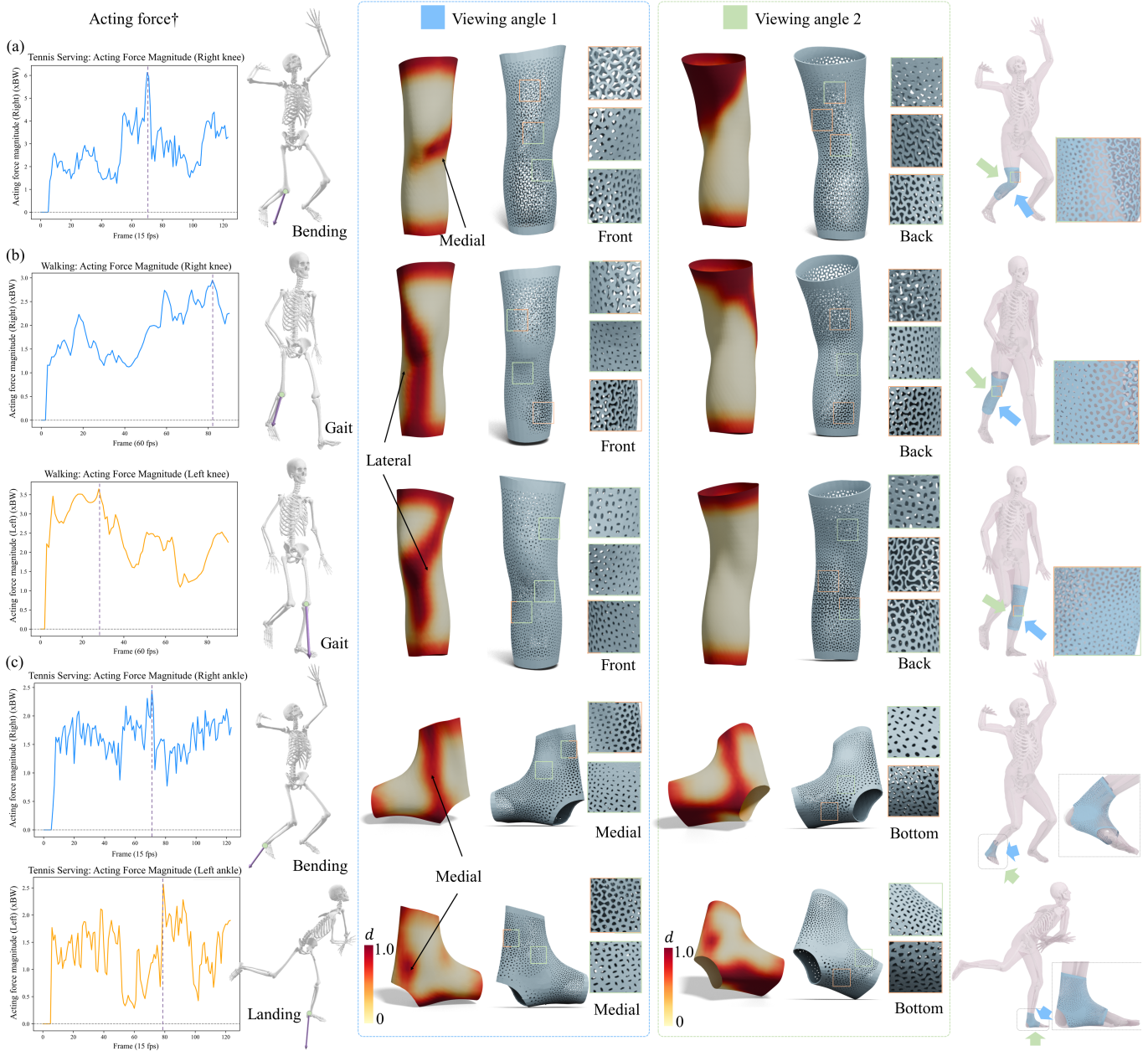
Fig. 9. We present a collection of designed prophylactic braces, demonstrating the capability of the pipeline for designing braces for different joint dynamics and varied movement patterns. The columns are: (far-left) magnitude of time-variant acting force given by the joint contact forces and muscle forces; (second-far-left) peak acting forces on the joint; (middle) optimized design variable field and a detailed view of the braces' distributed microstructures from two different angles; (right) showcase of optimized design on the simulated human body of the same frame. Zoom-in views for firm (green) and soft (orange) regions are marked in boxes. (a) Compared with the left prophylactic knee brace for tennis motion (Fig.1), we yield different structure designs for the right side due to the asymmetry of human motion and different loads acting on the body. (b) Gait example: our optimizer generates more lateral support on the knee to help stabilize the joint and prevent lateral movement during walking. (c) Landing impact after tennis serve creates higher loads acting on the ankle joint. The designs for the left ankle specifically address the impact of bending and landing motions, which can significantly increase the risk of ankle injuries. The design result aims to provide protection for the medial sides of the foot that aims to mitigate eversion angles. (†The magnitude of the acting force are plotted.)

tennis serving, with protocols introduced in Fig. 6(a). Our optimized design is compared against unbraced conditions, wearing unoptimized (uniformly firm) and commercial braces, as shown in Fig. 6. We demonstrate that the braces with the optimized distribution of elasticity can help reduce the risk of injury by preserving the flexibility of movement within the sagittal plane (Column 1, 3 from Table. 3) while reducing the frontal angles (Column 2, 4 from Table. 3).

8 CONCLUSION AND DISCUSSION

We present a motion-driven neural optimizer that leverages biomechanical insights and physical formulation for the topology design of prophylactic braces tailored to human motions. The generated results are validated via physical tests, demonstrating tailor-made mechanical protection and preservation of the optimized braces.

Our approach has several limitations that should be acknowledged. First, the mesh density and quality used for FEA could impact the accuracy of the simulation results. Second, classifying a model into soft/firm regions introduces significant simplification, and more sophisticated methods using more microstructures can further improve the optimization results. Third, the shape of the brace is derived from a human body model created by fitting a SKEL model onto a scan, which may introduce errors. Additionally, the study simplifies the analysis by neglecting FEA on bone structures and not accounting for changes in muscle forces due to reaction forces generated by different brace elasticities. These simplifications and potential errors could influence the accuracy and prevent the generation of further optimized braces. Future work should address these limitations to improve the precision of the results.

REFERENCES

Geoffrey D Abrams, Per A Renstrom, and Marc R Safran. 2012. Epidemiology of musculoskeletal injury in the tennis player. *British Journal of Sports Medicine* 46, 7 (2012), 492–498. https://doi.org/10.1136/bjsports-2012-091164 arXiv:https://bjsm.bmj.com/content/46/7/492.full.pdf

Michael Skipper Andersen and John Rasmussen. 2023. Chapter 7 - AnyBody modeling system. In *Digital Human Modeling and Medicine*, Gunther Paul and Mohamed

Hamdy Doweidar (Eds.). Academic Press, 143–159. https://doi.org/10.1016/B978-0-12-823913-1.00007-5

Joel Andersson, Joris Gillis, Greg Horn, James Rawlings, and Moritz Diehl. 2018. CasADi: a software framework for nonlinear optimization and optimal control. *Mathematical Programming Computation* 11 (07 2018). https://doi.org/10.1007/s12532-018-0139-4

Bruno Luiz Souza Bedo, Danilo S Catelli, Mario Lamontagne, and Paulo Roberto Pereira Santiago. 2020. A custom musculoskeletal model for estimation of medial and lateral tibiofemoral contact forces during tasks with high knee and hip flexions. *Computer methods in biomechanics and biomedical engineering.* 23, 10 (2020).

Javier Bonet and Richard D Wood. 2008. *Nonlinear Continuum Mechanics for Finite Element Analysis.* Cambridge University Press. https://doi.org/10.1017/CBO9780511755464

Jinhu Cai, Long Huang, Hongyu Wu, and Lairong Yin. 2023. Concurrent topology optimization of multiscale structure under uncertain dynamic loads. *International Journal of Mechanical Sciences* 251 (2023), 108355. https://doi.org/10.1016/j.ijmecsci.2023.108355

Aaditya Chandrasekhar and Krishnan Suresh. 2021. TOuNN: Topology optimization using neural networks. *Structural and Multidisciplinary Optimization* 63, 3 (2021), 1135–1149.

Desai Chen, Mélina Skouras, Bo Zhu, and Wojciech Matusik. 2018. Computational discovery of extremal microstructure families. *Science advances* 4, 1 (2018), eaao7005.

Heng Chi, Yuyu Zhang, Tsz Ling Elaine Tang, Lucia Mirabella, Livio Dalloro, Le Song, and Glaucio H. Paulino. 2021. Universal machine learning for topology optimization. *Computer Methods in Applied Mechanics and Engineering* 375 (2021), 112739. https://doi.org/10.1016/j.cma.2019.112739

Scott L. Delp, Frank C. Anderson, Allison S. Arnold, Peter Loan, Ayman Habib, Chand T. John, Eran Guendelman, and Darryl G. Thelen. 2007. OpenSim: Open-Source Software to Create and Analyze Dynamic Simulations of Movement. *IEEE Transactions on Biomedical Engineering* 54, 11 (2007), 1940–1950. https://doi.org/10.1109/TBME.2007.901024

Antoine Falisse, Gerard Serrancolí, Christopher L. Dembia, Jean-Baptiste Gillis, and Friedl De Groote. 2019. Algorithmic differentiation improves the computational efficiency of OpenSim-based trajectory optimization of human movement. *PLOS ONE* 14, 10 (2019), e0217730. https://doi.org/10.1371/journal.pone.0217730

Kelley E. Farwell, Cameron J. Powden, Meaghan R. Powell, Cailee W. McCarty, and Matthew C. Hoch. 2013. The Effectiveness of Prophylactic Ankle Braces in Reducing the Incidence of Acute Ankle Injuries in Adolescent Athletes: A Critically Appraised Topic. *Journal of Sport Rehabilitation* 22, 2 (2013), 137–142. https://doi.org/10.1123/jsr.22.2.137

Yusen Feng, Xiyan Xu, and Libin Liu. 2023. MuscleVAE: Model-Based Controllers of Muscle-Actuated Characters. In *SIGGRAPH Asia 2023 Conference Papers (SA '23).* Association for Computing Machinery, New York, NY, USA, Article 3, 11 pages. https://doi.org/10.1145/3610548.3618137

Simeon Gill, Steven Hayes, and Christopher J. Parker. 2016/11. 3D Body Scanning: Towards Shared Protocols for Data Collection- Addressing the needs of the body scanning community for ensuring comparable data collection. In *Proceedings of the 6th International Workshop of Advanced Manufacturing and Automation.* Atlantis Press, 281–284. https://doi.org/10.2991/iwama-16.2016.53

Michael T. Gross and Hsin-Yi Liu. 2003. The Role of Ankle Bracing for Prevention of Ankle Sprain Injuries. *Journal of Orthopaedic & Sports Physical Therapy* 33, 10 (2003), 572–577. https://doi.org/10.2519/jospt.2003.33.10.572

Austin Hagan, Diana Rocchio, Jaeho Shim, Jonathan Rylander, and Darryn Willoughby. 2024. Effects of Prophylactic Lace-Up Ankle Braces on Kinematics of the Lower Extremity During a State of Fatigue. *International Journal of KInesiology and Sports Science* 12, 1 (2024). https://doi.org/10.7575/aiac.ijkss.v.12n.1p.24

Xingjian Han, Benjamin Senderling, Stanley To, Deepak Kumar, Emily Whiting, and Jun Saito. 2023. GroundLink: A Dataset Unifying Human Body Movement and Ground Reaction Dynamics. In *ACM SIGGRAPH Asia 2023 Conference Proceedings.* 1–10.

HAS Motion, Inc. 2024. *Visual3D.* HAS Motion, Inc. https://www.has-motion.ca/ Originally developed by C-Motion, Inc., https://c-motion.com/.

Jakob S Jensen. 2009. Space–time topology optimization for one-dimensional wave propagation. *Computer Methods in Applied Mechanics and Engineering* 198, 5-8 (2009), 705–715.

Jingchao Jiang, Yi Xiong, Zhiyuan Zhang, and David W Rosen. 2022. Machine learning integrated design for additive manufacturing. *Journal of Intelligent Manufacturing* 33, 4 (2022), 1073–1086.

Manuel Kaufmann, Velko Vechev, and Dario Mylonopoulos. 2022. . https://doi.org/10.5281/zenodo.1234

Marilyn Keller, Keenon Werling, Soyong Shin, Scott Delp, Sergi Pujades, C. Karen Liu, and Michael J. Black. 2023. From Skin to Skeleton: Towards Biomechanically Accurate 3D Digital Humans. In *ACM ToG, Proc. SIGGRAPH Asia*, Vol. 42.

Carolin Körner and Yvonne Liebold-Ribeiro. 2014. A systematic approach to identify cellular auxetic materials. *Smart Materials and Structures* 24, 2 (2014), 025013.

Phill-Seung Lee and Klaus-Jürgen Bathe. 2004. Development of MITC isotropic triangular shell finite elements. *Computers & Structures* 82, 11 (2004), 945–962.

https://doi.org/10.1016/j.compstruc.2004.02.004

Zachary F. Lerner, Matthew S. DeMers, Scott L. Delp, and Raymond C. Browning. 2015. How tibiofemoral alignment and contact locations affect predictions of medial and lateral tibiofemoral contact forces. *Journal of Biomechanics* 48, 4 (2015), 644–650. https://doi.org/10.1016/j.jbiomech.2014.12.049

Bruno Lévy, Sylvain Petitjean, Nicolas Ray, and Jérome Maillot. 2023. Least squares conformal maps for automatic texture atlas generation. In *Seminal Graphics Papers: Pushing the Boundaries, Volume 2*. 193–202.

Yue Li, Stelian Coros, and Bernhard Thomaszewski. 2023. Neural Metamaterial Networks for Nonlinear Material Design. *ACM Trans. Graph.* 42, 6, Article 186 (dec 2023), 13 pages. https://doi.org/10.1145/3618325

Baoshou Liu, Xiaoming Wang, Zhuo Zhuang, and Yinan Cui. 2023a. Dynamic concurrent topology optimization and design for layer-wise graded structures. *Composite Structures* 319 (2023), 117190. https://doi.org/10.1016/j.compstruct.2023.117190

Baoshou Liu, Xiaoming Wang, Zhuo Zhuang, and Yinan Cui. 2023b. Dynamic concurrent topology optimization and design for layer-wise graded structures. *Composite Structures* 319 (2023), 117190.

Hsueh-Ti Derek Liu. 2018. *Blender Toolbox*. https://github.com/HTDerekLiu/BlenderToolbox

Martin Majewski, Susanne Habelt, and Klaus Steinbrück. 2006. Epidemiology of athletic knee injuries: A 10-year study. *Knee* 13, 3 (2006), 184–188. https://doi.org/10.1016/j.knee.2006.01.005

S Senthil Murugan. 2020. Mechanical properties of materials: definition, testing and application. *Int. J. Mod. Stud. Mech. Eng* 6, 2 (2020), 28–38.

Gregory D Myer, Kevin R Ford, Jane Khoury, Paul Succop, and Timothy E Hewett. 2011. Biomechanics laboratory-based prediction algorithm to identify female athletes with high knee loads that increase risk of ACL injury. *British Journal of Sports Medicine* 45, 4 (2011), 245–252. https://doi.org/10.1136/bjsm.2009.069351

Wenliang Qian, Yang Xu, and Hui Li. 2023. A topology description function-enhanced neural network for topology optimization. *Computer-Aided Civil and Infrastructure Engineering* 38, 8 (2023), 1020–1040.

Arash Radman, Xiaodong Huang, and YM Xie. 2013. Topology optimization of functionally graded cellular materials. *Journal of Materials Science* 48 (2013), 1503–1510.

Christian Schumacher, Steve Marschner, Markus Gross, and Bernhard Thomaszewski. 2018. Mechanical characterization of structured sheet materials. *ACM Trans. Graph.* 37, 4, Article 148 (jul 2018), 15 pages. https://doi.org/10.1145/3197517.3201278

Ole Sigmund. 1994. Materials with prescribed constitutive parameters: an inverse homogenization problem. *International Journal of Solids and Structures* 31, 17 (1994), 2313–2329.

Ole Sigmund. 2001. A 99 line topology optimization code written in Matlab. *Structural and multidisciplinary optimization* 21 (2001), 120–127.

Saketh Sridhara, Aaditya Chandrasekhar, and Krishnan Suresh. 2022. A generalized framework for microstructural optimization using neural networks. *Materials & Design* 223 (2022), 111213.

Robert W Sumner and Jovan Popović. 2004. Deformation transfer for triangle meshes. *ACM Transactions on graphics (TOG)* 23, 3 (2004), 399–405.

Salvatore Torquato. 2010. Optimal design of heterogeneous materials. *Annual review of materials research* 40 (2010), 101–129.

Brian H. H. Tuang, Zheng Qin Ng, Joshua Z. Li, and Dinesh Sirisena. 2023. Biomechanical Effects of Prophylactic Knee Bracing on Anterior Cruciate Ligament Injury Risk: A Systematic Review. *Clinical Journal of Sport Medicine* 33, 1 (January 2023), 78–89. https://doi.org/10.1097/JSM.0000000000001052

Velko Vechev, Ronan Hinchet, Stelian Coros, Bernhard Thomaszewski, and Otmar Hilliges. 2022a. Computational Design of Active Kinesthetic Garments. In *Proceedings of the 35th Annual ACM Symposium on User Interface Software and Technology* (Bend, OR, USA) (UIST '22). Association for Computing Machinery, New York, NY, USA, Article 23, 11 pages. https://doi.org/10.1145/3526113.3545674

Velko Vechev, Ronan Hinchet, Stelian Coros, Bernhard Thomaszewski, and Otmar Hilliges. 2022b. Computational Design of Active Kinesthetic Garments. In *Proceedings of the 35th Annual ACM Symposium on User Interface Software and Technology*. 1–11.

Velko Vechev, Juan Zarate, Bernhard Thomaszewski, and Otmar Hilliges. 2022c. Computational design of kinesthetic garments. In *Computer Graphics Forum*, Vol. 41. Wiley Online Library, 535–546.

E A L M Verhagen and K Bay. 2010. Optimising ankle sprain prevention: A critical review and practical appraisal of the literature. *Britich Journal of Sports Medicine* (2010). https://doi.org/10.1136/bjsm.2010.076406

Charlie C.L. Wang and Yong Chen. 2013. Thickening freeform surfaces for solid fabrication. *Rapid Prototyping Journal* 19, 6 (2013), 395–406.

Charlie C.L. Wang and Dinesh Manocha. 2013. GPU-based offset surface computation using point samples. *Computer-Aided Design* 45, 2 (2013), 321–330. https://doi.org/10.1016/j.cad.2012.10.015 Solid and Physical Modeling 2012.

Charlie C.L. Wang and Kai Tang. 2007. Woven model based geometric design of elastic medical braces. *Computer-Aided Design* 39, 1 (2007), 69–79.

Weiming Wang, Dirk Munro, Charlie CL Wang, Fred van Keulen, and Jun Wu. 2020. Space-time topology optimization for additive manufacturing: Concurrent optimization of structural layout and fabrication sequence. *Structural and Multidisciplinary Optimization* 61 (2020), 1–18.

Seth Watts, William Arrighi, Jun Kudo, Daniel A Tortorelli, and Daniel A White. 2019. Simple, accurate surrogate models of the elastic response of three-dimensional open truss micro-architectures with applications to multiscale topology design. *Structural and Multidisciplinary Optimization* 60 (2019), 1887–1920.

Keenon Werling, Nicholas A. Bianco, Michael Raitor, Jon Stingel, Jennifer L. Hicks, Steven H. Collins, Scott L. Delp, and C. Karen Liu. 2023. AddBiomechanics: Automating model scaling, inverse kinematics, and inverse dynamics from human motion data through sequential optimization. *bioRxiv* (2023). https://doi.org/10.1101/2023.06.15.545116 arXiv:https://www.biorxiv.org/content/early/2023/09/08/2023.06.15.545116.full.pdf

Jonas Zehnder, Yue Li, Stelian Coros, and Bernhard Thomaszewski. 2021. Ntopo: Mesh-free topology optimization using implicit neural representations. *Advances in Neural Information Processing Systems* 34 (2021), 10368–10381.

Lihi Zelnik-Manor and Pietro Perona. 2004. Self-tuning spectral clustering. *Advances in neural information processing systems* 17 (2004).

Xiaoting Zhang, Guoxin Fang, Chengkai Dai, Jouke Verlinden, Jun Wu, Emily Whiting, and Charlie C.L. Wang. 2017. Thermal-Comfort Design of Personalized Casts. In *Proceedings of the 30th Annual ACM Symposium on User Interface Software and Technology* (Québec City, QC, Canada) (UIST '17). Association for Computing Machinery, New York, NY, USA, 243–254. https://doi.org/10.1145/3126594.3126600

Yunbo Zhang and Tsz-Ho Kwok. 2019. Customization and topology optimization of compression casts/braces on two-manifold surfaces. *Computer-Aided Design* 111 (2019), 113–122.

Zeyu Zhang, Yu Li, Weien Zhou, Xiaoqian Chen, Wen Yao, and Yong Zhao. 2021. TONR: An exploration for a novel way combining neural network with topology optimization. *Computer Methods in Applied Mechanics and Engineering* 386 (2021), 114083.

Bo Zhu, Mélina Skouras, Desai Chen, and Wojciech Matusik. 2017. Two-scale topology optimization with microstructures. *ACM Transactions on Graphics (TOG)* 36, 4 (2017), 1.

A NOTATION TABLE

We provide a full list of notations employed in our main manuscript in Table.4

Table 4. List of symbols employed in the paper

Term	Explanation
β	the shape parameters of SKEL model [Keller et al. 2023]
$\mathbf{q}$	the pose parameters of SKEL model [Keller et al. 2023]
e	the finite elements in FEA
$\mathbf{K}$	the global stiffness matrix for FEA
$\mathbf{k}_0$	the element's stiffness matrix of MITC3 shell
$\mathbf{U}$	the nodal displacement vector for FEA
$\mathbf{u}_e$	the nodal displacement of an element e
$\mathbf{F}_{GRF}$	the ground reaction force
$\mathbf{F}_{acting}$	the overall acting force
$\mathbf{F}_{JCF}$	the joint contact forces
$\sum \mathbf{F}_{mus}$	the sum of the muscle forces
$d(u, v)$	NN based design function in the domain
d_i	the value of design variable on the i-th node of the mesh $\mathcal{M}$

Continued from previous column

Term	Explanation
d_e	the design variable sampled at the center of an element e
f_E	the function of the Young's modulus
f_V	the function of the volume ratio
V_e	the volume of an element e
N_l	the number of elements
N_t	the number of frames
t_i	the i-th time frame
ϕ	the joint angles of the human body
W_c	the discrete compliance on an element e
W_e	the elastic energy on an element e as defined in Eq. 4
G_e	the deformation gradient of an element e
A_e	the relative area change of an element e
C_e	the right Cauchy-Green tensor of an element e
I_e	the first invariant of the right Cauchy-Green tensor of an element e
λ_e	the Lamé's first parameter of an element e
μ_e	the shear modulus of an element e
ν	the Poisson's ratio
f_{cell}	the distance field to the skeletons in a unit parametric domain
f_M	the implicit solid of the distributed microstructures in the domain
$f_{\bar{M}}$	the blended implicit solid of the soft and firm microstructures in the domain
f_{seg}	the blending map for recognizing soft and firm regions
$f_{M,soft}$	the implicit solid of the soft microstructures in the domain
$f_{M,firm}$	the implicit solid of the firm microstructures in the domain
$f_{\bar{E}}$	the blended Young's modulus function of the soft and firm microstructures in the domain
$f_{E,soft}$	the Young's modulus function of the soft microstructures
$f_{E,firm}$	the Young's modulus function of the firm microstructures
N_w	the number of neurons
w_i	the i-th neural weight
Φ_i	the Gaussian covariance
ω_i	the loss weight of the i-th loss term
$S_{preserve}$	set of DoFs that need to be preserved (e.g. sagittal angles)
$S_{prevent}$	set of DoFs that need to be controlled (e.g. frontal angles)
$\dot{\phi}_s$	the updated joint angle for s given the reaction as defined in Eq. 3
ϕ_s	the target joint angle for s
p	the parameter for p-norm method ($p = 20$ in our trials)
$\mathcal{D}$	the pairs of corresponding points on the cutting line

Concluded